Toward Practical Gas Sensing with Highly Reduced Graphene Oxide: A New Signal Processing Method To Circumvent Run-to-Run and Device-to-Device Variations

Ganhua Lu,[†] Sungjin Park,[‡] Kehan Yu,[†] Rodney S. Ruoff,[‡] Leonidas E. Ocola,[§] Daniel Rosenmann,[§] and Junhong Chen[†,*]

[†]Department of Mechanical Engineering, University of Wisconsin—Milwaukee, 3200 North Cramer Street, Milwaukee, Wisconsin 53211, United States, [‡]Department of Mechanical Engineering and the Texas Materials Institute, University of Texas at Austin, 204 East Dean Keeton, Austin, Texas 78712, United States, and [§]Center for Nanoscale Materials, Argonne National Laboratory, 9700 South Cass Avenue, Argonne, Illinois 60439, United States

Nanoscaled materials, such as carbon nanotubes (CNTs) and nanowires, are candidates for chemical sensing and biosensing elements to be deployed in compact, low-power, and portable sensors and sensor arrays.[1−3] Graphene, a two-dimensional (2-D) monolayer of sp^2-bonded carbon atoms[4] exhibiting exceptional mechanical,[5] thermal,[6] and electrical[4,7] properties, holds interest for sensing as every atom is a surface atom and charge carrier transport through graphene is highly sensitive to adsorption/desorption of molecules; for example, graphene is a promising material for both gas sensing[8−13] and biosensing.[14,15] Graphene-based sensors can detect gas adsorption down to the single-molecule level,[8] with the mechanism stated to be charge transfer induced by adsorption/desorption of gaseous molecules (which act as electron donors or acceptors) on the graphene surface, leading to changes in the graphene conductance.[8]

Graphene can be produced by various approaches including micromechanical exfoliation of graphite,[7,16] epitaxial growth,[17] chemical vapor deposition (CVD),[18−20] exfoliation of graphite in liquid solvents,[21] and direct synthesis of "graphene powder" by plasma-enhanced CVD.[22] These graphenes are all possible choices for graphene-based devices. Another low-cost choice is to use reduced graphene oxide (R-GO) platelets. Graphite oxide can be made in large scale and can be readily dispersed in water to form graphene oxide.[23] The basal plane and edges of graphene oxide platelets are

ABSTRACT Graphene is worth evaluating for chemical sensing and biosensing due to its outstanding physical and chemical properties. We first report on the fabrication and characterization of gas sensors using a back-gated field-effect transistor platform with chemically reduced graphene oxide (R-GO) as the conducting channel. These sensors exhibited a 360% increase in response when exposed to 100 ppm NO_2 in air, compared with thermally reduced graphene oxide sensors we reported earlier. We then present a new method of signal processing/data interpretation that addresses (i) sensing devices with long recovery periods (such as required for sensing gases with these R-GO sensors) as well as (ii) device-to-device variations. A theoretical analysis is used to illuminate the importance of using the new signal processing method when the sensing device suffers from slow recovery and non-negligible contact resistance. We suggest that the work reported here (including the sensor signal processing method and the inherent simplicity of device fabrication) is a significant step toward the real-world application of graphene-based chemical sensors.

KEYWORDS: graphene · reduced graphene oxide · gas sensor · sensing performance · field-effect transistor

decorated with oxygen functional groups,[24−26] rendering them hydrophilic but electrically insulating.[27] By exposing such platelets to reductants such as hydrazine[28] or $NaBH_4$,[29] through thermal treatments,[11,30,31] or *via* UV-assisted photocatalysis,[32] electrically conductive R-GO platelets can be obtained. Colloids of R-GO in organic solvents such as ethanol and dimethylformamide (DMF) can be used for graphene-based device fabrication.[33]

Hydrazine-reduced graphene oxide has been studied for detection of acetone, warfare agents, and explosive agents at parts per billion concentrations with noise levels lower than CNT-based sensors.[9] Sensors using spin-coated, single-layer films of R-GO platelets exhibited temperature-dependent responses to NO_2 and NH_3.[10] The influence

of photoresist residue (left on mechanically exfoliated graphene surface following electrode fabrication) on graphene sensing was reported, as well.[34] We have reported on a sensing device using thermally reduced graphene oxide.[11,12] Despite the growing interest and rapid progress in graphene/R-GO sensors, there are, however, technical challenges that need to be addressed before they can be practically employed. The sensing signal or sensitivity of a gas sensor is conventionally defined as the relative change in the device resistance or conductance.[9,10,13] However, the time for graphene-based sensors to recover after a sensing event is relatively long at ambient conditions. If the sensor is not fully recovered, the sensing signal often declines or drifts from one sensing cycle to the next, making the sensing response unrepeatable even under the same analyte concentration and the conventional sensitivity formulation incapable of predicting the analyte concentration accurately. In addition, sensing performance differs from device to device even though the same fabrication process is followed and all graphene/R-GO materials are from the same batch. The contact resistance normally existing between the sensing material and the metal electrode further distorts the conventional sensitivity formulation.

Here we propose a new sensing signal processing/data interpretation method (i) to circumvent the run-to-run variation in sensing performance caused by insufficient recovery for individual R-GO sensors and (ii) to deal with common variations among R-GO devices due to various fabrication factors, such as differences in contact resistances, amount of R-GO platelets, and R-GO configurations on metal electrodes. We fabricate room-temperature gas sensors using R-GO on a field-effect transistor (FET) platform (Figure 1a,b) and characterize the sensing properties of R-GO devices for detecting low-concentration NO_2 and NH_3 gases in nearly practical gaseous environments (i.e., under atmospheric pressure, in dry air background, and at room temperature). We intentionally control the device recovery time, in conjunction with a simplified analytical model, to illustrate the effectiveness of our proposed signal processing method in comparison with the conventional sensitivity formulation. This signal processing method could potentially pave the way for the real-life application of graphene-based gas sensors and may also be useful for other nanomaterial-based sensors, such as CNT sensors.

RESULTS AND DISCUSSION

Preparation of R-GO Devices. The R-GO suspension (0.3 mg/mL; solvent: DMF/H_2O with volume ratio = 9) was prepared using a procedure previously reported (see details in Methods).[33] The as-synthesized R-GO platelets were mostly ~1 nm thick based on numerous atomic force microscopy (AFM) measurements.[33] Elemental analysis by the combustion of R-GO samples

indicated a C/O atomic ratio of 11.0, which is much higher than that for graphene oxide samples (1.2).[33] Figure 1c is a transmission electron microscopy (TEM) image of an individual R-GO platelet (with a lateral dimension of ~1.5 μm) supported on holey carbon film. The R-GO platelet had folds and rolls on its edges. A folded corner of the platelet is highlighted by a dashed rectangle with a zoom-in view shown in the lower-right inset of Figure 1c. The platelet edge indicated by a red arrow was further inspected using high-resolution TEM (HRTEM) (the top-left inset of Figure 1c) and showed multiple fringes in parallel caused by the rolls on the edge. Figure 1d is a selected area diffraction (SAD) pattern from the R-GO platelet in Figure 1c, exhibiting diffraction spots with hexagonal configuration typical of graphene. The SAD pattern of a graphene sheet can help reveal the number of layers in the sheet. Single-layer graphene structures display higher diffraction intensities for diffraction spots of inner hexagon than outer hexagon.[22,35,36] Shown in Figure 1e is the intensity profile of the diffraction spots labeled in the SAD pattern of Figure 1d. The relative intensities of the inner diffraction spots (−1010 and 0−110) were higher than those of the outer diffraction spots (−2110 and 1−210), indicating the single-layer nature of the R-GO platelet and confirming the successful restoration of most graphitic carbon during the reduction process.

R-GO devices were readily prepared by dispersing the R-GO suspension onto Au interdigitated electrodes prefabricated on the top of a Si wafer with a 200 nm thick thermally formed oxide layer and drying with compressed air flow, similar to the method used in our previous work on thermally reduced graphene oxide sensors.[11,12] A few drops of the R-GO suspension were cast onto Au interdigitated electrodes, resulting in a network of R-GO platelets (by bottom-contact with the substrate) on the Au fingers after solvent evaporation. The R-GO network serves as the conducting channel between the drain and source electrodes. The as-fabricated R-GO devices are sensitive to gaseous species without any further treatment and can be used for gas detection by simply measuring the change in the device resistance upon exposure to various gases.

Figure 1b shows a scanning electron microscopy (SEM) image of a network of R-GO platelets bridging a pair of neighboring Au electrode fingers. The R-GO platelets have lateral dimensions from a few hundred nanometers to ~1 μm, which agrees with previous AFM observations.[33] The edges of the R-GO sheets demonstrate higher contrast than the central area (Figure 1c), which may be due to the rolls and/or folds as observed in the TEM imaging. The arrangement of R-GO platelets on the electrode was quite random due to the arbitrary nature of the drop-casting process.

Gas Sensing with R-GO Devices. The gas sensing performance of as-fabricated R-GO devices was characterized under nearly practical conditions (i.e., room temperature,
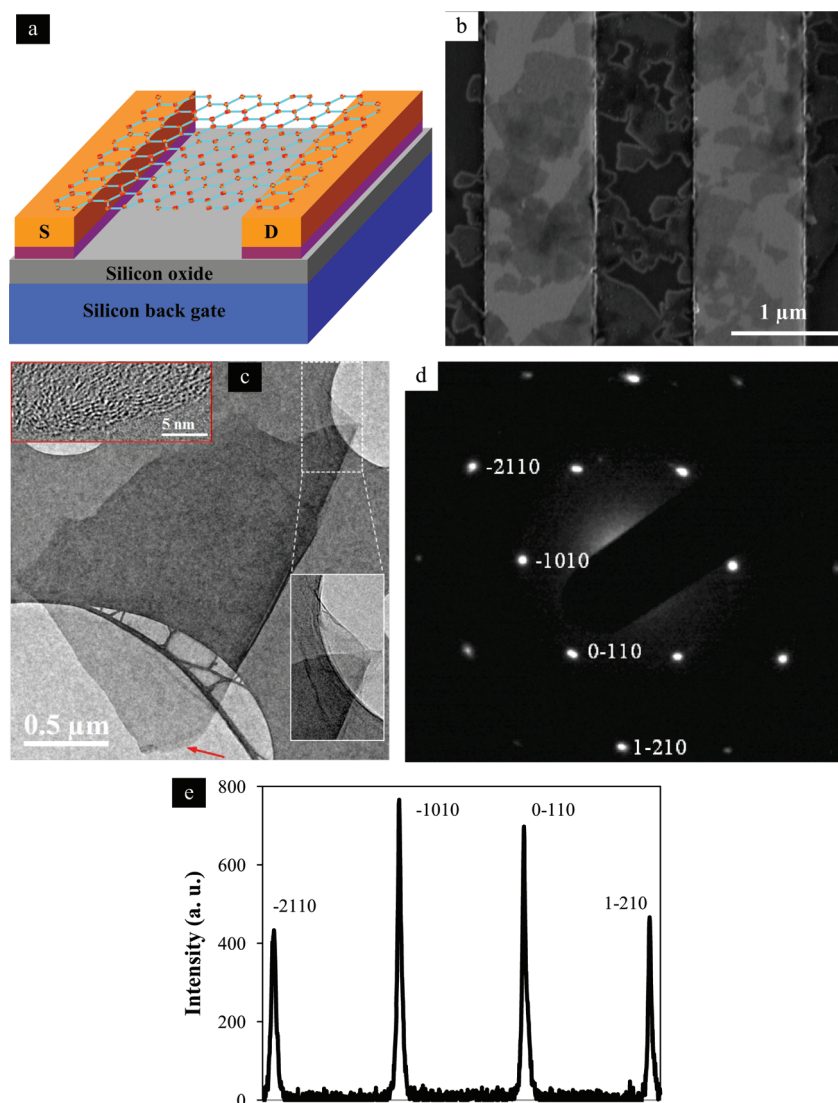
Figure 1. (a) Schematic of the R-GO device with an FET platform; the R-GO serves as the conducting channel by bridging the source and drain electrodes; the back of the Si wafer is used as the gate electrode. (b) SEM image of a sensing device composed of R-GO platelets that bridge neighboring Au fingers. (c) TEM image of an individual R-GO platelet supported on holey carbon film; the top-left inset is an HRTEM image showing the rolled edge of the sheet marked by the red arrow; the dashed rectangle indicates a folded corner of the R-GO platelet, which is more clearly shown in the lower-right inset. (d) SAD pattern from the R-GO platelet shown in c. (e) Intensity profile of the diffraction spots labeled in d; the relative intensities of the inner diffraction spots (−1010 and 0−110) were higher than those of the outer diffraction spots (−2110 and 1−210), indicating the single-layer nature of the R-GO platelet.

atmospheric pressure, and dry, clean air as reference gas environment) against low-concentration NO_2 and NH_3 diluted in dry air. The as-fabricated R-GO devices showed fairly strong responses to 100 ppm NO_2 and 1% NH_3, implying the large change in the electrical conductance of R-GO platelets. To compare the sensing response among R-GO devices, we used the normalized resistance as the sensor sensitivity that is defined as R_a/R_g for NO_2 detection and R_g/R_a for NH_3 sensing, where R_a is the device resistance in air and R_g the device resistance in the target gas (NO_2 or NH_3 diluted in air).

Figure 2a is a typical dynamic response (R_a/R_g vs time) of an R-GO device for room-temperature detection of 100 ppm NO_2. The sensor was mounted in an airtight test chamber with electrical feedthroughs[11,12,37]

and sequentially exposed to clean dry air flow (2 lpm) for 10 min to record a base value of the sensor conductance, 100 ppm NO_2 diluted in air (2 lpm) for 15 min to register a sensing signal, and clean air flow (2 lpm) again for 25 min to recover the device. The dashed curve specifies the 100 ppm NO_2 flow rate. Upon the introduction of NO_2, the sensor resistance went down, that is, the conductance of the sensor increased; when NO_2 flow was turned off and the air flow restored, the device started to re-establish its initial resistance.

The response curve during the NO_2 exposure can be clearly divided into two regimes that are distinguished by a fast response (sharp slope) and a slow response (moderate slope), which is consistent with the results reported by Robinson et al.[9] They attributed the fast
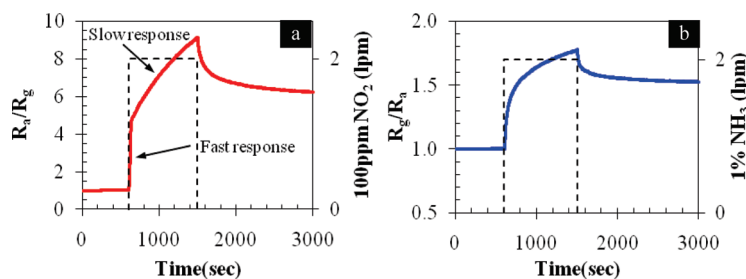
Figure 2. Representative dynamic behavior of R-GO sensors for (a) 100 ppm NO$_2$ and (b) 1% NH$_3$ detection.

response to molecular adsorption onto binding sites with low energy, such as sp^2-bonded carbon, while the slow response to interactions between gaseous molecules and high-energy binding sites (*e.g.*, vacancies, defects, and oxygen functional groups).[9] The maximum response (R_a/R_g) of this R-GO device to 100 ppm NO$_2$ is ~9.15, about 3.6 times higher than the thermally reduced GO sensor (~2.56) that we previously reported.[11] However, unlike thermally reduced GO sensors, which could recover from 100 ppm NO$_2$ exposure within ~30 min air exposure, R-GO devices typically could not regain the initial resistance with 25 min air exposure. Increasing the reduction level of graphene oxide could lead to more graphitic carbon atoms, vacancies, and defects, all of which provide more binding sites for molecular adsorption and enhance the sensing response; however, high-energy binding sites could delay recovery.[9] This slower recovery is unfavorable for R-GO sensors; however, it offered us an opportunity to explore the cycle-to-cycle variation for individual R-GO sensors and led to a new strategy to address the run-to-run deviation (to be discussed later).

The R-GO devices responded to NH$_3$, as well. Figure 2b shows the 1% NH$_3$ sensing data obtained from another R-GO device. Upon NH$_3$ exposure, the device resistance increased by ~1.7-fold, whereas the response of thermally reduced graphene oxide sensors we reported previously was ~1.3.[12] The recovery of the R-GO device after NH$_3$ sensing is quite slow, similar to that after NO$_2$ exposure; however, this recovery is much improved compared with thermally reduced graphene oxide sensors.[12]

The significantly improved sensitivity of chemically reduced GO reported here is mainly attributed to its higher reduction level compared with our previously reported thermally reduced GO. Chemical reduction and thermal treatments could produce R-GO with different atomic structure and chemical composition. The chemically reduced GO used in the present work had a C/O atomic ratio of 11.0, indicating a significant oxygen reduction.[33] In our previous work,[11,12] we used low-temperature (400 °C at maximum), atmospheric pressure thermal treatments to reduce graphene oxide in Ar, which could only lead to a moderate reduction level. Yang *et al.*[38] reported that the C/O atomic ratio of thermally treated graphene oxide in Ar at atmospheric

pressure increases to ~3.9, ~ 6.8, and ~11.36 after 200, 500, and 1000 °C annealing, respectively. The higher reduction level of the R-GO used in this study is thus responsible for its improved sensitivity as further reduction of GO could result in more adsorption sites on R-GO for analyte molecules. In addition, new functional chemical groups could be introduced to graphene sheets during chemical reduction. For example, trace amount of N—C groups are typically found in R-GO reduced with hydrazine as the reducing agent.[38] However, it is unclear whether those nitrogen-containing functional groups introduced during the chemical reduction affect the sensing behavior of R-GO. The different sensing behavior for chemically reduced and thermally reduced graphene oxide deserves further investigation.

The Hall measurements conducted by Novoselov and co-workers revealed that NO$_2$ serves as electron acceptor while NH$_3$ acts as electron donor upon adsorption onto graphene.[8] We found that R-GO demonstrates p-type semiconducting behavior in air; thus, the sensing response of R-GO is most likely due to the adsorption of NO$_2$ (NH$_3$) that enhances (lowers) the hole concentration in R-GO, thereby decreasing (increasing) the R-GO resistance.

Electronic Characterization of R-GO FETs. The transport characteristics of R-GO devices can be strongly influenced by the gas adsorption. Panels a and b of Figure 3 illustrate the transport characteristics of an R-GO device before any sensing tests and after the analyte (NO$_2$/NH$_3$) exposure (immediately measured at the end of a sensing cycle). The I_{ds}–V_g curves (I_{ds} is the drain–source current; V_g is the gate voltage) were obtained with the device stored in ambient conditions. Before gas sensing, the R-GO device demonstrated a threshold voltage (V_{th}) at about +20 V and p-dominated conductance within the V_g scan range (±40 V) and for both upward and downward V_g scans. This p-dominated semiconducting behavior agrees with the results acquired for room-environment exposed graphene prepared by micromechanical cleavage of graphite,[39] and chemical,[40] and thermal[11,31] reduction of graphene oxide. The p-type behavior could be attributed to the polarization of adsorbed molecules (*e.g.*, water) and/or defects introduced on the graphene sheets during the preparation or reduction process.[41] The observed hysteresis for I_{ds}–V_g curves is typical of
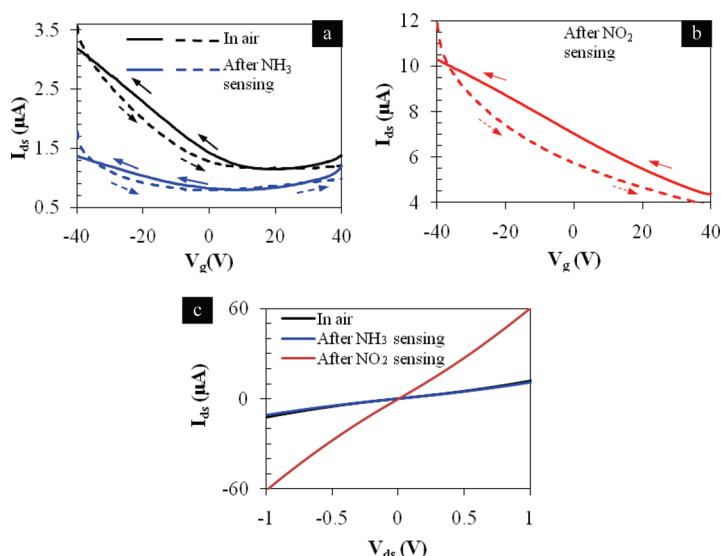
Figure 3. Transport characteristics (I_{ds}–V_g) of an R-GO device (a) before any sensing and at the end of an NH$_3$ sensing cycle; (b) after an NO$_2$ sensing cycle (V_{ds} = 0.1 V). (c) I_{ds}–V_{ds} curves before sensing, after NH$_3$, and after NO$_2$ sensing.

back-gated CNT and graphene FETs and is generally ascribed to the polarization of adsorbed molecules (such as water) in the applied electric field.[31,42,43]

Figure 3a also includes the I_{ds}–V_g curves obtained immediately after an NH$_3$ sensing cycle (10 min air/15 min 1% NH$_3$/and 25 min air); the curves are almost symmetric (v-shaped) with V_{th} at about 0 V, indicating the ambipolar characteristic of the device after the NH$_3$ exposure. The conductance of the device at V_g = 0 slightly decreased, which is consistent with the incomplete recovery at the end of the sensing cycle, as shown in Figure 2b. NH$_3$ could serve as an n-type dopant, leading to a lowered hole density and the shift of the threshold voltage toward the negative regime.[43] In contrast, Figure 3b shows that NO$_2$ exposure not only rendered the R-GO device completely p-type within the V_g scan range (evidenced by a significant shift of V_{th} toward a much more positive V_g) but also significantly increased its conductance. NO$_2$ has an unpaired electron and is a strong oxidizer with electron-withdrawing power.[44] The electron transfer from R-GO to NO$_2$ could increase free hole density in R-GO, thereby enhancing its conductance. In addition, because of their polarity, NH$_3$ and NO$_2$ adsorbed on R-GO could contribute to the hysteresis behavior of I_{ds}–V_g curves.

The shift of transport curves could be used to estimate the total charge transfer (ΔQ) using $\Delta Q = C \Delta V_{th}$,[45,46] where C is the SiO$_2$ gate capacitance and ΔV_{th} is the shift of the threshold voltage V_{th} for the R-GO FET device. Assuming negligible change in the capacitance C, the more dramatic change in V_{th} after NO$_2$ sensing suggests that more charge transfer occurs between NO$_2$ and R-GO than that between NH$_3$ and R-GO even with the NH$_3$ concentration (1%) much higher than NO$_2$ (100 ppm). Our observation agreed with the first-principles study[44] that estimated higher

charge transfer between NO$_2$ and graphene than that between NH$_3$ and graphene.

Figure 3c compares the I_{ds}–V_{ds} (V_{ds} is the drain–source bias) curves before and after sensing. The conductance of the R-GO device slightly decreased after the NH$_3$ sensing, while it was still more than 3-fold higher than that in air after NO$_2$ sensing. These curves are symmetric and mostly linear, which could imply possible Ohmic contact between R-GO sheets and metal electrodes. The V_{th} shift after the NO$_2$/NH$_3$ exposure (Figure 3a,b) would have been unlikely if a Schottky contact had dominated the R-GO FET. Single-walled CNTs (SWCNTs) can be regarded as seamless cylinders by rolling up graphene sheets.[1] It was found that Au can make good Ohmic contact with p-type SWCNTs with a contact resistance of about 10–50 kΩ.[47] Contact resistance of similar magnitude may be expected for graphene and Au since CNT and graphene are closely related. Furthermore, compared with the cylinder-plane contact for SWCNTs bottom-contacted with the electrode, the planar contact area between an R-GO platelet and the Au electrode is relatively larger, which could lower contact resistance. The conductance of the air-dried R-GO used in our study is ~1700 S/m,[33] which corresponds with an estimated resistance of ~590 kΩ for a 1 nm thick square R-GO platelet with 1 μm sides. The junctions formed between R-GO platelets could also add to the resistance of R-GO platelet network. The resistance of R-GO devices is most likely dominated by R-GO platelets; therefore, we speculate that the contact has limited role in the sensing process and that the charge transfer between the analyte (NO$_2$/NH$_3$) and the R-GO primarily contributes to the sensing response. We also performed preliminary measurements to estimate the contact resistance between R-GO and Au and found that the

R-GO resistance indeed dominated the device resistance (see section 1 in Supporting Information).

A New Signal Processing Method for R-GO Sensors. The room-temperature sensing performance of the R-GO devices under atmospheric pressure is very encouraging for practical applications when considering the simplicity and low cost to fabricate these devices and the potential opportunities for optimization. However, the as-fabricated R-GO sensors have recovery problems common to CNT-, graphene-, and nanowire-based gas sensors operating at room temperature because the thermal energy is usually insufficient to overcome the activation energy for desorption.[48] Insufficient recovery of a sensor can cause unreliable sensing outputs. For instance, when it was used to continuously monitor 100 ppm NO_2, an SWCNT sensor (see details in section 2 of Supporting Information) gave drifting signal (Figure S2c) if full recovery was not achieved before the next sensing cycle, causing gradual degradation in its response (R_a/R_g) (Figure S2d). The sensing signal could also be incorrectly amplified when switching from one analyte to another (*e.g.*, the sensitivity of NO_2 could be enlarged if the device had not fully recovered from the previous NH_3 sensing). Figure 4a shows eight sets of data using an R-GO sensor for 100 ppm NO_2 detection. The normalized sensing response (R_a/R_g) varied within a wide range when the waiting time between successive cycles differed from a few minutes (partial recovery) to a few days (full recovery), implying that the use of the conventional sensitivity definition could lead to inaccuracy in signal interpretation. UV illumination and heating are frequently suggested methods to accelerate the recovery process of these room-temperature sensors; however, integrating a heater or a UV source into a micro- or nanoscale sensor, if ever possible, increases the complexity in the device design and fabrication and the cost.

We have developed a new signal processing/data interpretation method to circumvent the run-to-run variation caused by incomplete recovery of R-GO devices. Instead of using the ratio of resistance before and after sensing, the new method suggests that $|R_a-R_g|$ *versus* R_a plot could be a more reliable indicator of the analyte concentration. Note that we use R_a-R_g *versus* R_a for NO_2 and R_g-R_a *versus* R_a for NH_3 sensing in the following discussion; NO_2 or NH_3 can be identified by the sign of R_g-R_a. We plotted in Figure 4b the data points of (R_a-R_g) *versus* R_a from the eight tests of 100 ppm NO_2 sensing, whose R_a/R_g *versus* time curves are shown in Figure 4a. Interestingly, a linear relation seems to exist between R_a-R_g and R_a, as supported by a correlation coefficient of ~0.999. We then tested the same R-GO sensor for 50 ppm NO_2 detection and found another linear R_a-R_g *versus* R_a curve, which has a more moderate slope and smaller intercept compared with that of 100 ppm NO_2. We speculate that the slope is associated with the NO_2 concentration because a horizontal curve

should correspond with clean air without NO_2 (*i.e.*, $R_a-R_g = 0$ without NO_2 exposure). The change in the intercept could be caused by the contact resistance, as will be discussed later.

We used another R-GO sensor to inspect the relation of R_g-R_a *versus* R_a for NH_3 sensing. The six curves of R_g/R_a *versus* time for 1% NH_3 sensing in Figure 4c demonstrate obvious run-to-run deviations caused by incomplete recovery between cycles; however, similar to the case of NO_2 sensing, the R_g-R_a *versus* R_a data for 1% and 0.5% NH_3 sensing (Figure 4d) both suggest a linear relationship with the correlation coefficients being 0.979 and 0.996, respectively. The slope of the R_g-R_a *versus* R_a curve varies with the NH_3 concentration.

Theoretical Analysis on the Relation between $|R_a-R_g|$ and R_a. We carried out preliminary analysis to inspect the relation between $|R_a-R_g|$ and R_a and to evaluate the feasibility to use the proposed signal processing method for practical operation of R-GO sensors. Assuming that the overall resistance of an R-GO device is the sum of the total resistance of the R-GO platelets (R_{R-GO}) and the total contact resistance (R_C) between the R-GO and Au electrodes, the initial resistance of the device in air (R_a) and the device resistance in a target gas (R_g) are $R_a = R_{R-GO,a} + R_{C,a}$ and $R_g = R_{R-GO,g} + R_{C,g}$, respectively. Here, the subscripts "a" and "g" designate resistances in air and in target gas, respectively. We next analyze R_a-R_g, R_a, and their correlation when an R-GO sensor is used for NO_2 sensing (the analysis of R_g-R_a *vs* R_a for NH_3 sensing can be carried out in a similar fashion). The change in the overall resistance of the R-GO sensor for a given NO_2 exposure can be expressed as

$$R_a - R_g = (R_{R-GO,a} - R_{R-GO,g}) + (R_{C,a} - R_{C,g}) \quad (1)$$

The charge transfer between R-GO and NO_2 can be interpreted using the adsorption model proposed by Strano and co-workers.[49,50] If we assume that (i) the charge carrier density (n) is reversely proportional to the available binding sites on R-GO surface (*i.e.*, NO_2 adsorption leads to a higher carrier density, or $n_g > n_a$; n_a and n_g are the charge carrier density of R-GO in air and in NO_2, respectively) and that (ii) the surface coverage (θ_{R-GO}) of gaseous molecules on R-GO determines the amount of occupied binding sites and leads to the conductance change, we can get

$$\theta_{R-GO} \propto \frac{n_g - n_a}{n_a} \quad (2)$$

If we further assume a proportionality constant δ, which is related to the analyte concentration and the exposure time, eq 2 becomes

$$\delta \times \theta_{R-GO} = \frac{n_g - n_a}{n_a} \quad (3)$$

The resistance change of R-GO can also be written as

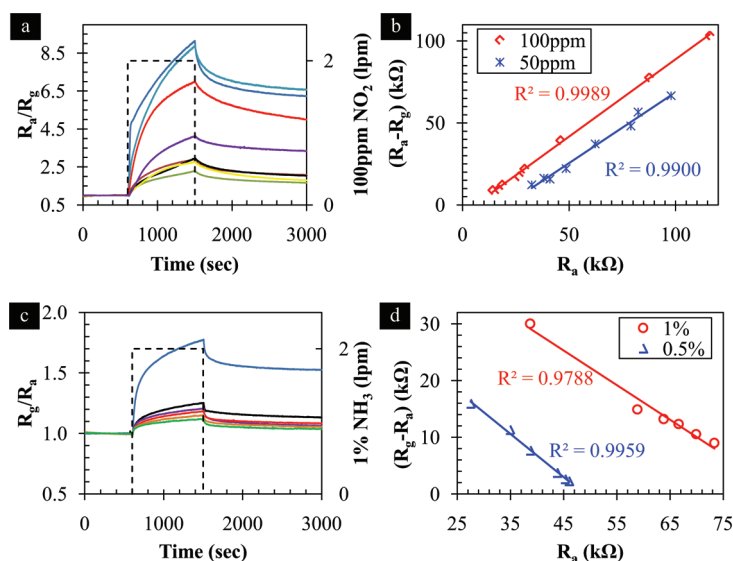$$R_{R-GO,a} - R_{R-GO,g} = R_{R-GO,a}\left(1 - \frac{R_{R-GO,g}}{R_{R-GO,a}}\right) \quad (4)$$

Figure 4. Run-to-run variations of two R-GO devices for (a) 100 ppm NO$_2$ (eight runs) and (c) 1% NH$_3$ (six runs) sensing. (b) Plot of $R_a - R_g$ vs R_a for 100 ppm and 50 ppm NO$_2$ sensing. (d) Plot of $R_g - R_a$ vs R_a for 1% and 0.5% NH$_3$ sensing.

Substituting eq 3 and $R_{R\text{-}GO,g}/R_{R\text{-}GO,a} = n_a/n_g$ into eq 4 yields

$$R_{R\text{-}GO,a} - R_{R\text{-}GO,g} = R_{R\text{-}GO,a}\left(\frac{\delta\theta_{R\text{-}GO}}{1 + \delta\theta_{R\text{-}GO}}\right)$$

$$= B \times R_{R\text{-}GO,a} \qquad (5)$$

where $B = \delta\theta_{R\text{-}GO}/(1 + \delta\theta_{R\text{-}GO})$ is constant for a given analyte concentration and a given exposure time. B is in fact determined by the sensing properties of R-GO because it directly links with the charge transfer between R-GO and analytes.

It was pointed out that the change in the charge carrier density $(n_g - n_a)$ of graphene depended linearly on the analyte concentration under given exposure conditions.[8] If the sensing response is solely from the gas adsorption on R-GO and there is no contact resistance ($R_C = 0$), we then have

$$\frac{R_a - R_g}{R_a} = \frac{R_{R\text{-}GO,a} - R_{R\text{-}GO,g}}{R_{R\text{-}GO,a}} = B \qquad (6)$$

Hence, the correlation of $R_g - R_a$ versus R_a is a straight line that crosses (0,0) and has a slope B dependent on the analyte concentration for a given exposure time. If eq 6 could hold true, the ratio of $R_g - R_a$ to R_a, which is often used in the literature, would be ideal to evaluate the sensing response regardless of the sensor recovery. However, contact resistance between graphene and the electrode is inevitable most of the time ($R_C \neq 0$), which causes serious issues (e.g., signal drift) for using eq 6 to precisely assess sensing in practical usage even if the sensing is dominated by the change in the conductance of sensing elements (e.g., R-GO).

We next discuss the case that the contact resistance between the R-GO and the metal electrode is non-negligible ($R_C \neq 0$) but considerably lower than R-GO resistance (i.e., $R_C \ll R_{R\text{-}GO}$, as we have speculated that

the R-GO resistance contributes mostly to the total device resistance). If the sensing is mainly due to charge transfer between R-GO and analytes, it would be reasonable to assume that the change in R_C is insignificant (i.e., $R_{C,a} \approx R_{C,g}$) compared with the change in $R_{R\text{-}GO}$. Then the overall resistance change $(R_g - R_a)$ of the R-GO device is

$$R_a - R_g \approx R_{R\text{-}GO,a} - R_{R\text{-}GO,g} \qquad (7)$$

Therefore, with eqs 5 and 7, we get

$$(R_a - R_g)/R_a = B \times R_{R\text{-}GO,a}/(R_{R\text{-}GO,a} + R_{C,a}) \qquad (8)$$

Since $R_C \ll R_{R\text{-}GO,a}$, we have

$$(R_a - R_g)/R_a = B/(1 + R_C/R_{R\text{-}GO,a})$$
$$\approx B(1 - R_C/R_{R\text{-}GO,a}) \qquad (9)$$

and

$$R_a - R_g = BR_a - \frac{BR_C}{R_{R\text{-}GO,a}}(R_{R\text{-}GO,a} + R_C)$$

$$\approx BR_a - BR_C \qquad (10)$$

Equation 10 results in a straight line with a slope of B that depends on NO$_2$ concentration and a nonzero intercept of $(-BR_C)$ that relates to the contact resistance. It is worth pointing out that, based on eq 10, the intercept term $(-BR_C)$ makes $(R_a - R_g)/R_a$ problematic for accurate evaluation of the sensing response if the sensor has recovery or stability issues (i.e., R_a varies from one test to another). Specifically, the right-hand side of eq 10 becomes $(B - BR_C/R_a)$ when divided by R_a. Although B would stay constant under given sensing conditions, (BR_C/R_a) changes with varying R_a even if change in R_C is presumably negligible. Above analysis suggests that, for $(R_a - R_g)/R_a$ to be a reliable indicator of senor sensitivity, either R_C needs to be eliminated or unvarying R_a is required. The contact between graphene and metal electrodes seems largely inevitable

for an electronic device to function. Complete recovery of graphene sensors at room temperature is time-consuming (on the scale of tens of minutes or even hours) without extra assistance such as heating or UV illumination. In this regard, using the plot of R_g-R_a versus R_a provides an effective and reliable approach to indicating the R-GO sensor sensitivity.

A further examination of eq 10 suggests that contact resistance R_C could be estimated from a curve of R_g-R_a versus R_a, which could be very useful when direct measurements of R_C are difficult. Applying eq 10 to the 100 ppm NO_2 curve in Figure 4b yields a value of ~5.5 kΩ for R_C. Since R_a ranges between ~15 and ~120 kΩ for that curve, the fact that $R_{R-GO,a}$ is about 2−20 times larger than R_C validates the above analysis for the most R_a range. Of course, the R_a-R_g versus R_a curve is more reliable for larger R_a values. Because of $R_a = R_C + R_{R-GO,a}$ and negligible change in R_C, a higher value of R_a implies bigger weight of $R_{R-GO,a}$ in the overall resistance, ensuring the validity of the assumption of $R_C \ll R_{R-GO,a}$. On the other hand, for NO_2 sensing, R_a of a given R-GO sensor could be seen as an indication of available adsorption sites with a larger R_a meaning better recovery and/or more available adsorption sites for NO_2.

Both the experimental data and the theoretical analysis indicate that the linear curve of $|R_a-R_g|$ versus R_a can be used as an effective signal processing method to circumvent the run-to-run variations of the R-GO sensors, paving the way for their practical applications. Specifically, the new signal processing method can be implemented through an initial calibration procedure followed by a look-up procedure. In the calibration procedure, one can first operate a sensor at each concentration for a specific analyte, record R_a and R_g for multiple times, and then assemble a calibration chart by plotting the set of $|R_a-R_g|$ versus R_a curves, each corresponding with a certain analyte concentration. In a real detection, one could extract a concentration of an analyte by locating the point of $(R_a, |R_a-R_g|)$ on the calibration chart after R_a and R_g are measured. We schematically illustrate the proposed calibration and look-up procedures in Figure 5 with NO_2 sensing as an example. First, multiple sensing tests (e.g., with various incomplete recovery cycles) are performed for a given NO_2 concentration (e.g., 100 ppm), resulting in data for the R_a-R_g versus R_a curve corresponding to 100 ppm NO_2. Second, similar sensing tests are conducted for a different NO_2 concentration (e.g., 80 ppm), providing data for the curve of 80 ppm NO_2. After finishing tests with the interested concentration range of the sensor (e.g., 100 to 10 ppm), all the R_a-R_g versus R_a curves can be assembled into a calibration chart (Figure 5a), which will be used as a database for the sensor operation. In a practical operation of the R-GO sensor, the sensor resistance in air is recorded as R_a before any NO_2 sensing. After the NO_2 exposure for the

same duration as in the calibration process, the sensor resistance is recorded as R_g. A data point in the calibration chart can then be positioned using R_a and R_a-R_g and the NO_2 concentration can be obtained, as shown in Figure 5b. Similar procedures can be followed to implement the new method for detection of other analytes (e.g., NH_3). We note that the same signal processing method could be useful for gas sensors based on CNTs (see Figure S2 in Supporting Information) or nanowires.

We also used the relation revealed in eq 10 to address the device-to-device variation caused by non-uniformity among R-GO devices due to factors such as the varying amount and changing configuration of R-GO platelets. As an example, we show in Figure 6a the R_a/R_g versus time curves from seven R-GO devices for 100 ppm NO_2 sensing. The response R_a/R_g differs from one device to another; however, using data from Figure 6a, we can obtain a very linear curve of R_a-R_g versus R_a, as shown in Figure 6b. This linear curve can be used to address the non-uniformity among R-GO devices and for optimizing R-GO devices. A higher value of R_a/R_g is still preferred for a sensor because it offers a wider range in which the sensor can provide more reliable signals (e.g., if the change in resistance of a sensor is too small, it will be difficult to accurately evaluate signals induced by low-concentration gases). Techniques such as spin-coating[10] and dielectrophoretic assembly[51] have the potential to reduce the variation among devices and enhance the consistency in device characteristics with better control over the number of R-GO platelets and the layout of platelets on the electrode. However, before a reliable method to suppress the device-to-device variation is found, the proposed correlation will be useful to interpret the sensing data from R-GO devices.

Our signal processing method for R-GO sensors has been derived for a sensing mechanism based on adsorption/desorption-induced charge transfer. Therefore, the method could be useful for similar sensors (e.g., CNT sensors) operating with the same mechanism. Of course, an appropriate signal processing approach will heavily rely on the fundamental understanding of the sensing element (e.g., graphene, CNTs, or nanowires) and the associated sensing mechanism (e.g., charge transfer, chemical gating effect, or Schottky contact). New signal processing methods may need to be sought for sensors featuring long recovery and significant contact resistance but operating with a sensing mechanism other than charge transfer.

CONCLUSIONS

We have demonstrated gas sensors using chemically R-GO as the conducting channel on a back-gated FET platform. R-GO in an ambient environment showed p-dominated semiconducting behavior based on transport measurements. The R-GO sensors were
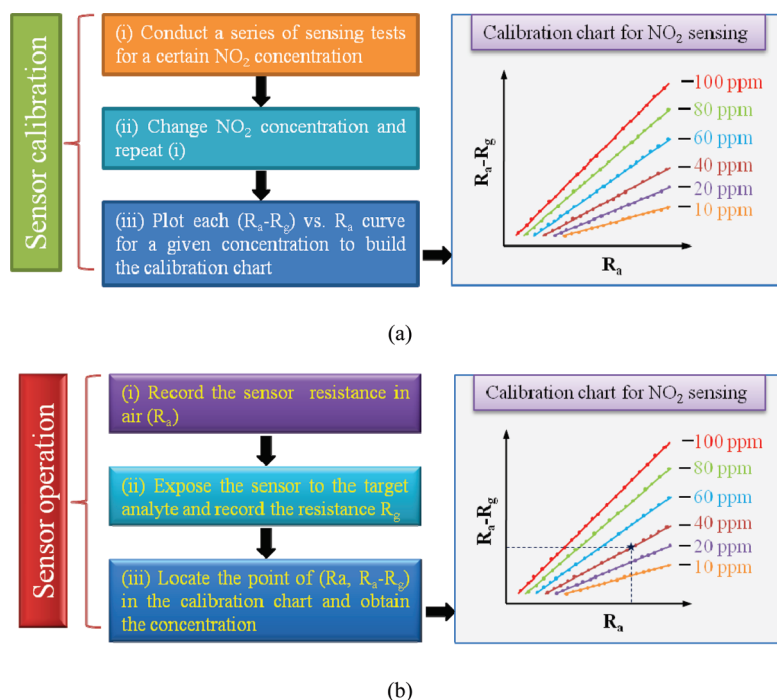
Figure 5. Implementation of the proposed signal processing method for NO$_2$ detection using R-GO sensors. (a) Initial calibration procedure; and (b) look-up procedure for actual operation.
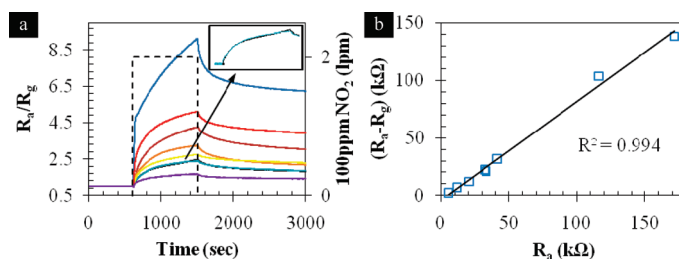

Figure 6. (a) R_a/R_g *vs* time curves from seven R-GO devices used for 100 ppm NO$_2$ sensing. The response R_a/R_g varies widely from one device to another. (b) $R_a - R_g$ *vs* R_a data of the seven devices shows a linear correlation.

highly responsive to low-concentration NO$_2$ and NH$_3$ gases diluted in air, exhibiting higher sensitivity than sensors based on thermally reduced graphene oxide that we reported earlier. The sensing response could be attributed mainly to the charge transfer between R-GO and adsorbed gaseous molecules (NO$_2$/NH$_3$). Both experiments and theoretical analysis indicate that the slope of the $|R_a - R_g|$ *versus* R_a plot is a more reliable indicator of the analyte concentration than the conventional sensi-

tivity formulation. This new signal processing method can be used to effectively circumvent the run-to-run variation caused by incomplete recovery of R-GO devices during the real sensing deployment and the device-to-device variation among R-GO sensors commonly seen even with the same fabrication procedure. Other nanomaterial-based gas sensors that suffer from slow recovery and deviations among devices may also benefit from such a data interpretation method.

METHODS

Preparation of R-GO. The R-GO suspension was prepared using a procedure previously reported.[33] First, graphite oxide was synthesized by the oxidative treatment of purified natural graphite (SP-1, Bay Carbon, MI) through the modified Hummers method.[52] A stable suspension of graphene oxide platelets was then obtained by adding graphite oxide in water (3 mg of

graphite oxide per mL of H$_2$O) followed by 1 h ultrasonication. The presence of oxygen functional groups makes graphene oxide platelets strongly hydrophilic and the aqueous dispersion stable.[28] After that, DMF was added into the graphene oxide suspension with a volume ratio of DMF/H$_2$O = 9, resulting in a graphene oxide concentration of 0.3 mg/mL. Hydrazine monohydrate was subsequently used to chemically reduce the graphene oxide suspension for 12 h at 80 °C with stirring, which

led to a homogeneous suspension of R-GO platelets. More details about synthesis and characterization of the R-GO can be found in ref 33.

R-GO Device Fabrication. The p-doped silicon wafer covered with a 200 nm thick thermally formed oxide layer was used as the substrate on the top of which the interdigitated electrodes were fabricated using an e-beam lithography process. The Au fingers (50 nm thick) of the electrode are ~1 μm wide and 1 μm apart. A 2 nm thick Cr layer was used to enhance the adhesion between the Au and the Si wafer. A few drops of the R-GO suspension were cast onto Au interdigitated electrodes, resulting in a suspended network of R-GO platelets (by bottom-contact with the substrate) left on the Au fingers after solvent evaporation. The R-GO network serves as the conducting channel between the drain and source electrodes. The as-fabricated R-GO devices are sensitive to gaseous species without any further treatment and can be used for gas detection by simply measuring the change in the device resistance upon exposure to various gases.

TEM and SEM. TEM analysis of R-GO sheets was carried out using a Hitachi H 9000 NAR TEM with a point resolution of 0.18 nm at 300 kV in the phase contrast HRTEM imaging mode. TEM samples were prepared by adding droplets of the R-GO suspension onto Cu TEM grids covered with holey carbon film. The morphology of R-GO devices was characterized using a field-emission SEM (Hitachi S 4800), which has a resolution of 1.4 nm at 1 kV acceleration voltage.

Electronic Characterization of R-GO Devices. Both current−voltage characteristics (I_{ds}−V_{ds}) and transport characteristics (I_{ds}−V_g) were performed on R-GO devices using a Keithley 2602 source meter. I_{ds}−V_{ds} curves of the R-GO device were measured by ramping drain−source voltage V_{ds} and simultaneously recording drain−source current I_{ds}. For transport measurements of R-GO devices, the back side of the silicon wafer was used as the gate electrode and a constant bias V_{ds} (0.1 V) was applied between the source−drain electrodes while sweeping the gate voltage V_g between −40 V and +40 V. V_g was scanned both upward (from −40 to +40 V) and downward (from +40 to −40 V) to inspect the hysteresis of R-GO devices.

Gas Sensing Characterization of R-GO Devices. The gas sensing performance of as-fabricated R-GO devices was characterized under nearly practical conditions (*i.e.*, room temperature, atmospheric pressure, and dry, clean air as reference gas environment) against low-concentration NO_2 and NH_3 diluted in dry air. NO_2 is a well-known gaseous pollutant from combustion processes. High levels of NH_3 can lead to adverse effects on human health and environment. The R-GO device was mounted in an airtight test chamber with electrical feedthroughs for gas sensing characterizations.[11,12,37] The chamber volume (~6.3 × 10^{-5} m³) was minimized to reduce the capacitive effect during the gas switching. Variations in the electrical resistance of the R-GO device were monitored when the device was periodically exposed to clean air and NO_2- or NH_3-laden air. Gas cylinders with certified analyte concentrations (100 ppm NO_2 or 1% NH_3) were purchased from Praxair.

A sensing test cycle typically comprises three successive periods in which the R-GO device was exposed to (1) clean air flow for 10 min to acquire a base value of the sensor conductance, (2) target gas for 15 min to register a sensing signal, and (3) clean air flow again for 25 min to recover the device. A low constant dc current (100 nA) was maintained between the source and drain electrodes of the device while the change in the dc source−drain bias was recorded.

Supporting Information Available: Analysis of contact resistance between R-GO and Au electrode, calibration results for an SWCNT sensor. This material is available free of charge *via* the Internet at http://pubs.acs.org.

REFERENCES AND NOTES

1. Baughman, R. H.; Zakhidov, A. A.; de Heer, W. A. Carbon Nanotubes—The Route toward Applications. *Science* **2002**, *297*, 787–792.

2. Ferrari, M. Cancer Nanotechnology: Opportunities and Challenges. *Nat. Rev. Cancer* **2005**, *5*, 161–171.

3. Kauffman, D. R.; Star, A. Carbon Nanotube Gas and Vapor Sensors. *Angew. Chem., Int. Ed.* **2008**, *47*, 6550–6570.

4. Geim, A. K.; Novoselov, K. S. The Rise of Graphene. *Nat. Mater.* **2007**, *6*, 183–191.

5. Frank, I. W.; Tanenbaum, D. M.; Van der Zande, A. M.; McEuen, P. L. Mechanical Properties of Suspended Graphene Sheets. *J. Vac. Sci. Technol., B* **2007**, *25*, 2558–2561.

6. Balandin, A. A.; Ghosh, S.; Bao, W. Z.; Calizo, I.; Teweldebrhan, D.; Miao, F.; Lau, C. N. Superior Thermal Conductivity of Single-Layer Graphene. *Nano Lett.* **2008**, *8*, 902–907.

7. Novoselov, K. S.; Geim, A. K.; Morozov, S. V.; Jiang, D.; Zhang, Y.; Dubonos, S. V.; Grigorieva, I. V.; Firsov, A. A. Electric Field Effect in Atomically Thin Carbon Films. *Science* **2004**, *306*, 666–669.

8. Schedin, F.; Geim, A. K.; Morozov, S. V.; Hill, E. W.; Blake, P.; Katsnelson, M. I.; Novoselov, K. S. Detection of Individual Gas Molecules Adsorbed on Graphene. *Nat. Mater.* **2007**, *6*, 652–655.

9. Robinson, J. T.; Perkins, F. K.; Snow, E. S.; Wei, Z. Q.; Sheehan, P. E. Reduced Graphene Oxide Molecular Sensors. *Nano Lett.* **2008**, *8*, 3137–3140.

10. Fowler, J. D.; Allen, M. J.; Tung, V. C.; Yang, Y.; Kaner, R. B.; Weiller, B. H. Practical Chemical Sensors from Chemically Derived Graphene. *ACS Nano* **2009**, *3*, 301–306.

11. Lu, G. H.; Ocola, L. E.; Chen, J. H. Gas Detection Using Low-Temperature Reduced Graphene Oxide Sheets. *Appl. Phys. Lett.* **2009**, *94*, 083111.

12. Lu, G. H.; Ocola, L. E.; Chen, J. H. Reduced Graphene Oxide for Room-Temperature Gas Sensors. *Nanotechnology* **2009**, *20*, 445502.

13. Dua, V.; Surwade, S. P.; Ammu, S.; Agnihotra, S. R.; Jain, S.; Roberts, K. E.; Park, S.; Ruoff, R. S.; Manohar, S. K. All-Organic Vapor Sensor Using Inkjet-Printed Reduced Graphene Oxide. *Angew. Chem., Int. Ed.* **2010**, *49*, 2154–2157.

14. He, Q. Y.; Sudibya, H. G.; Yin, Z. Y.; Wu, S. X.; Li, H.; Boey, F.; Huang, W.; Chen, P.; Zhang, H. Centimeter-Long and Large-Scale Micropatterns of Reduced Graphene Oxide Films: Fabrication and Sensing Applications. *ACS Nano* **2010**, *4*, 3201–3208.

15. Mao, S.; Lu, G. H.; Yu, K. H.; Bo, Z.; Chen, J. H. Specific Protein Detection Using Thermally Reduced Graphene Oxide Sheet Decorated with Gold Nanoparticle-Antibody Conjugates. *Adv. Mater.* **2010**, *22*, 3521–3526.

16. Lu, X. K.; Yu, M. F.; Huang, H.; Ruoff, R. S. Tailoring Graphite with the Goal of Achieving Single Sheets. *Nanotechnology* **1999**, *10*, 269–272.

17. Berger, C.; Song, Z. M.; Li, X. B.; Wu, X. S.; Brown, N.; Naud, C.; Mayou, D.; Li, T. B.; Hass, J.; Marchenkov, A. N.; *et al.* Electronic Confinement and Coherence in Patterned Epitaxial Graphene. *Science* **2006**, *312*, 1191–1196.

18. Reina, A.; Jia, X.; Ho, J.; Nezich, D.; Son, H.; Bulovic, V.; Dresselhaus, M. S.; Kong, J. Large Area, Few-Layer Graphene Films on Arbitrary Substrates by Chemical Vapor Deposition. *Nano Lett.* **2009**, *9*, 30–35.

19. Li, X.; Cai, W.; An, J.; Kim, S.; Nah, J.; Yang, D.; Piner, R.; Velamakanni, A.; Jung, I.; Tutuc, E.; *et al.* Large-Area Synthesis of High-Quality and Uniform Graphene Films on Copper Foils. *Science* **2009**, *324*, 1312–1314.

20. Bae, S.; Kim, H.; Lee, Y.; Xu, X.; Park, J.-S.; Zheng, Y.; Balakrishnan, J.; Lei, T.; Ri Kim, H.; Song, Y. I.; *et al.* Roll-to-Roll Production of 30-Inch Graphene Films for Transparent Electrodes. *Nat. Nanotechnol.* **2010**, *5*, 574–578.

21. Lotya, M.; Hernandez, Y.; King, P. J.; Smith, R. J.; Nicolosi, V.; Karlsson, L. S.; Blighe, F. M.; De, S.; Wang, Z. M.;

McGovern, I. T.; *et al.* Liquid Phase Production of Graphene by Exfoliation of Graphite in Surfactant/Water Solutions. *J. Am. Chem. Soc.* **2009,** *131*, 3611–3620.

22. Dato, A.; Radmilovic, V.; Lee, Z.; Phillips, J.; Frenklach, M. Substrate-Free Gas-Phase Synthesis of Graphene Sheets. *Nano Lett.* **2008,** *8*, 2012–2016.

23. Ruoff, R. Calling All Chemists. *Nat. Nanotechnol.* **2008,** *3*, 10–11.

24. Cai, W. W.; Piner, R. D.; Stadermann, F. J.; Park, S.; Shaibat, M. A.; Ishii, Y.; Yang, D. X.; Velamakanni, A.; An, S. J.; Stoller, M.; *et al.* Synthesis and Solid-State NMR Structural Characterization of C-13-Labeled Graphite Oxide. *Science* **2008,** *321*, 1815–1817.

25. Lerf, A.; He, H. Y.; Forster, M.; Klinowski, J. Structure of Graphite Oxide Revisited. *J. Phys. Chem. B* **1998,** *102*, 4477–4482.

26. He, H. Y.; Klinowski, J.; Forster, M.; Lerf, A. A New Structural Model for Graphite Oxide. *Chem. Phys. Lett.* **1998,** *287*, 53–56.

27. Park, S.; Ruoff, R. S. Chemical Methods for the Production of Graphenes. *Nat. Nanotechnol.* **2009,** *4*, 217–224.

28. Stankovich, S.; Piner, R. D.; Chen, X. Q.; Wu, N. Q.; Nguyen, S. T.; Ruoff, R. S. Stable Aqueous Dispersions of Graphitic Nanoplatelets *via* the Reduction of Exfoliated Graphite Oxide in the Presence of Poly(sodium 4-styrenesulfonate). *J. Mater. Chem.* **2006,** *16*, 155–158.

29. Muszynski, R.; Seger, B.; Kamat, P. V. Decorating Graphene Sheets with Gold Nanoparticles. *J. Phys. Chem. C* **2008,** *112*, 5263–5266.

30. Wang, X.; Zhi, L. J.; Mullen, K. Transparent, Conductive Graphene Electrodes for Dye-Sensitized Solar Cells. *Nano Lett.* **2008,** *8*, 323–327.

31. Jung, I.; Dikin, D. A.; Piner, R. D.; Ruoff, R. S. Tunable Electrical Conductivity of Individual Graphene Oxide Sheets Reduced at "Low" Temperatures. *Nano Lett.* **2008,** *8*, 4283–4287.

32. Williams, G.; Seger, B.; Kamat, P. V. TiO_2-Graphene Nanocomposites. UV-Assisted Photocatalytic Reduction of Graphene Oxide. *ACS Nano* **2008,** *2*, 1487–1491.

33. Park, S.; An, J. H.; Jung, I. W.; Piner, R. D.; An, S. J.; Li, X. S.; Velamakanni, A.; Ruoff, R. S. Colloidal Suspensions of Highly Reduced Graphene Oxide in a Wide Variety of Organic Solvents. *Nano Lett.* **2009,** *9*, 1593–1597.

34. Dan, Y. P.; Lu, Y.; Kybert, N. J.; Luo, Z. T.; Johnson, A. T. C. Intrinsic Response of Graphene Vapor Sensors. *Nano Lett.* **2009,** *9*, 1472–1475.

35. Meyer, J. C.; Geim, A. K.; Katsnelson, M. I.; Novoselov, K. S.; Booth, T. J.; Roth, S. The structure of Suspended Graphene Sheets. *Nature* **2007,** *446*, 60–63.

36. Wilson, N. R.; Pandey, P. A.; Beanland, R.; Young, R. J.; Kinloch, I. A.; Gong, L.; Liu, Z.; Suenaga, K.; Rourke, J. P.; York, S. J.; *et al.* Graphene Oxide: Structural Analysis and Application as a Highly Transparent Support for Electron Microscopy. *ACS Nano* **2009,** *3*, 2547–2556.

37. Lu, G. H.; Ocola, L. E.; Chen, J. H. Room-Temperature Gas Sensing Based on Electron Transfer between Discrete Tin Oxide Nanocrystals and Multiwalled Carbon Nanotubes. *Adv. Mater.* **2009,** *21*, 2487–2491.

38. Yang, D.; Velamakanni, A.; Bozoklu, G.; Park, S.; Stoller, M.; Piner, R. D.; Stankovich, S.; Jung, I.; Field, D. A.; Ventrice C. A., Jr.; *et al.* Chemical Analysis of Graphene Oxide Films after Heat and Chemical Treatments by X-ray Photoelectron and Micro-Raman Spectroscopy. *Carbon* **2009,** *47*, 145–152.

39. Romero, H. E.; Shen, N.; Joshi, P.; Gutierrez, H. R.; Tadigadapa, S. A.; Sofo, J. O.; Eklund, P. C. n-Type Behavior of Graphene Supported on Si/SiO_2 Substrates. *ACS Nano* **2008,** *2*, 2037–2044.

40. Gilje, S.; Han, S.; Wang, M.; Wang, K. L.; Kaner, R. B. A Chemical Route to Graphene for Device Applications. *Nano Lett.* **2007,** *7*, 3394–3398.

41. Kim, K.; Park, H. J.; Woo, B. C.; Kim, K. J.; Kim, G. T.; Yun, W. S. Electric Property Evolution of Structurally Defected Multilayer Graphene. *Nano Lett.* **2008,** *8*, 3092–3096.

42. Kim, W.; Javey, A.; Vermesh, O.; Wang, O.; Li, Y. M.; Dai, H. J. Hysteresis Caused by Water Molecules in Carbon Nanotube Field-Effect Transistors. *Nano Lett.* **2003,** *3*, 193–198.

43. Lohmann, T.; von Klitzing, K.; Smet, J. H. Four-Terminal Magneto-Transport in Graphene p−n Junctions Created by Spatially Selective Doping. *Nano Lett.* **2009,** *9*, 1973–1979.

44. Leenaerts, O.; Partoens, B.; Peeters, F. M. Adsorption of H_2O, NH_3, CO, NO_2, and NO on Graphene: A First-Principles Study. *Phys. Rev. B* **2008,** *77*, 125416.

45. Hecht, D. S.; Ramirez, R. J. A.; Briman, M.; Artukovic, E.; Chichak, K. S.; Stoddart, J. F.; Gruner, G. Bioinspired Detection of Light Using a Porphyrin-Sensitized Single-Wall Nanotube Field Effect Transistor. *Nano Lett.* **2006,** *6*, 2031–2036.

46. Peng, N.; Zhang, Q.; Chow, C. L.; Tan, O. K.; Marzari, N. Sensing Mechanisms for Carbon Nanotube Based NH_3 Gas Detection. *Nano Lett.* **2009,** *9*, 1626–1630.

47. Yaish, Y.; Park, J. Y.; Rosenblatt, S.; Sazonova, V.; Brink, M.; McEuen, P. L. Electrical Nanoprobing of Semiconducting Carbon Nanotubes Using an Atomic Force Microscope. *Phys. Rev. Lett.* **2004,** *92*, 046401.

48. Fan, Z. Y.; Lu, J. G. Gate-Refreshable Nanowire Chemical Sensors. *Appl. Phys. Lett.* **2005,** *86*, 123510.

49. Lee, C. Y.; Strano, M. S. Understanding the Dynamics of Signal Transduction for Adsorption of Gases and Vapors on Carbon Nanotube Sensors. *Langmuir* **2005,** *21*, 5192–5196.

50. Lee, C. Y.; Baik, S.; Zhang, J. Q.; Masel, R. I.; Strano, M. S. Charge Transfer from Metallic Single-Walled Carbon Nanotube Sensor Arrays. *J. Phys. Chem. B* **2006,** *110*, 11055–11061.

51. Vijayaraghavan, A.; Sciascia, C.; Dehm, S.; Lombardo, A.; Bonetti, A.; Ferrari, A. C.; Krupke, R. Dielectrophoretic Assembly of High-Density Arrays of Individual Graphene Devices for Rapid Screening. *ACS Nano* **2009,** *3*, 1729–1734.

52. Park, S.; An, J.; Piner, R. D.; Jung, I.; Yang, D.; Velamakanni, A.; Nguyen, S. T.; Ruoff, R. S. Aqueous Suspension and Characterization of Chemically Modified Graphene Sheets. *Chem. Mater.* **2008,** *20*, 6592–6594.